Fermilab

MAIA: A new detector concept for a 10 TeV muon collider

FERMILAB-PUB-25-0058-PPD

arXiv:2502.00181

MAIA: A new detector concept for a 10 TeV muon collider

Charles Bell,[1] Daniele Calzolari,[2] Christian Carli,[2] Karri Folan Di Petrillo,[3] Micah Hillman,[1] Tova R. Holmes,[1] Sergo Jindariani,[4] Kiley E. Knnnedy,[5] Ka Hei Martin Kwok,[4] Anton Lechner,[2] Lawrence Lee,[1] Thomas Madlener,[6] Federico Meloni,[6] Isobel Ojalvo,[5] Priscilla Pani,[6] Rose Powers,[5] Benjamin Rosser,[3] Leo Rozanov,[3] Kyriacos Skoufaris,[2] Elise Sledge,[7] Alexander Tuna,[1] and Junjia Zhang[5]

[1]*University of Tennessee, Knoxville, TN, USA*
[2]*European Organization for Nuclear Research (CERN), Switzerland*
[3]*University of Chicago, IL, USA*
[4]*Fermi National Accelerator Laboratory, IL, USA*
[5]*Princeton University, NJ, USA*
[6]*Deutsches Elektronen-Synchrotron DESY, Germany*
[7]*California Institute of Technology, CA, USA*

Dated: February 4, 2025

Abstract

Muon colliders offer a compelling opportunity to explore the TeV scale and conduct precision tests of the Standard Model, all within a relatively compact geographical footprint. This paper introduces a new detector concept, MAIA (Muon Accelerator Instrumented Apparatus), optimized for $\sqrt{s} = 10$ TeV $\mu^+\mu^-$ collisions. The detector features an all-silicon tracker immersed in a 5T solenoid field. High-granularity silicon-tungsten and iron-scintillator calorimeters surrounding the solenoid capture high-energy electronic and hadronic showers, respectively, and support particle-flow reconstruction. The outermost subsystem comprises an air-gap muon spectrometer, which enables standalone track reconstruction for high-momentum muons. The performance of the MAIA detector is evaluated in terms of differential particle reconstruction efficiencies and resolutions. Beam-induced background (BIB) simulations generated in FLUKA are overlaid with single particle gun samples to assess detector reconstruction capabilities under realistic experimental conditions. Even with BIB, reconstruction efficiencies exceed 95% for energetic tracks, photons, and neutrons in the central region of the detector. This paper outlines promising avenues of future work, including forward region optimization and opportunities for enhanced flavor/boosted object tagging, and addresses the technological assumptions needed to achieve the desired detector performance.

CONTENTS

I. INTRODUCTION

Particle colliders have played a central role in experimentally testing the Standard Model (SM) of particle physics, from the discovery of the charm quark in 1974 to that of the Higgs boson in 2012 [1–4]. Over the past half-century, the hunt for new physics in collider experiments has alternated between two approaches: either direct searches for particles with higher masses or smaller couplings, or precision measurements of SM parameters to probe new physics indirectly. While the Large Hadron Collider (LHC) will remain at the forefront of the energy frontier of particle physics for the next twenty years, new colliders are essential to further our understanding of fundamental particle physics in the following decades.

Muon colliders are an appealing option for future particle accelerators due to their ability to reach high energies with a relatively compact size, high power efficiency, and low cost [5]. Extensive studies on the physics potential of multi-TeV muon colliders suggest that these machines offer competitive sensitivity to both the precision measurements of e^+e^- machines and the discovery potential of pp colliders with comparable parton center-of-mass energies [6, 7]. Various staging options for a TeV-scale muon collider have been proposed [7–10]. In one scenario currently being considered by the International Muon Collider Collaboration, an initial 3 TeV machine would be followed by a 10 TeV collider; in other scenarios, a 10 TeV machine would be built immediately but with run with lower luminosity to be upgraded over time. In both cases, reaching the 10 TeV scale offers an unprecedented reach in both energy and precision.

The primary challenge driving detector design $\mu^+\mu^-$ colliders is the reconstruction of a broad range of collision products-of-interest in the presence of beam-induced background (BIB) arising from muon decay along the beamline [11]. BIB consists primarily of TeV-scale electrons that interact with the accelerator and detector components. This process generates large multiplicities of predominantly soft secondary particles, some of which enter the detector volume. These secondary particles are typically out-of-time with respect to the beam collisions and do not originate at the interaction region. As a result, the presence of BIB imposes stringent demands on the granularity, resolution, and timing capabilities of muon collider detectors to effectively suppress background to acceptable levels without significantly degrading experimental performance. Additionally, radiation tolerance is crucial, as detectors must withstand moderate radiation doses induced by the beam.

Past studies of muon collider detectors, including those the context of previous R&D efforts such as the US Muon Accelerator Program (MAP), have mainly focused on lower center-of-mass energies [12–14]. More recently, comprehensive simulations of a 3 TeV muon collider detector, adapted from CLIC, have demonstrated robust performance [7]. However, the design optimized for 3 TeV collisions is inadequate for 10 TeV collisions due to significant differences in final state particle kinematics, such as energy, rapidity, and decay length. Furthermore, the particle spectrum and timing characteristics of the BIB are notably different between the two energy scales. Since no predecessor detector design exists specifically for 10 TeV leptonic collisions, it is critical to develop a design from first principles to serve as the basis for physics studies, leverage anticipated advancements in detector technologies, and maximize the physics potential of a collider at this energy scale. Key physics goals include precision tests of the Higgs boson and other SM parameters as well as excellent sensitivity to a broad range of exotic phenomena beyond the SM, underscoring the importance of developing a robust, general-purpose detector. This paper presents an initial detector concept for a 10 TeV muon collider and evaluates its preliminary performance. The design, called MAIA (Muon Accelerator Instrumented Apparatus), serves as an initial step in the evolution of lepton collider detectors toward the higher energy regime of 10 TeV collisions and beyond.

The structure of the paper is as follows: Section II details the detector simulation setup, while Section III provides an overview of the experimental conditions. The detector layout is described in Section IV, and the simulated performance results are presented in Section V. Future work and potential improvements are outlined in Section VI, with a brief summary provided in Section VII.

II. DETECTOR SIMULATION

Detector simulation and reconstruction were performed with the MUONCOLLIDERSOFT software stack [15, 16] within the Key4hep software ecosystem [17, 18]. This section summarizes the tools used for this study, including the custom modifications applied to existing Key4hep software packages.

The detector geometry was implemented for simulation with the DD4hep detector description toolkit [19], which also supplies the necessary interfaces to Geant4 [20] to simulate

the detector response via the `ddsim` [21] tool. Outputs are provided in both the LCIO [22] and the EDM4hep format [23], which is the standard event data model (EDM) used in Key4hep.

Reconstruction and large parts of the analysis chain are run using the Gaudi-based event processing framework of Key4hep. We use K4MARLINWRAPPER to run many existing components from previous studies developed inside the iLCSoft framework [24] using Marlin [25] and LCIO. These functionalities include a Combinatorial Kalman Filter (CKF) [26–28] based track reconstruction using version 13.0 of *A Common Tracking Software* (ACTS) [29] and dedicated digitization and overlay algorithms to handle BIB.

The simulation of the detector response for the BIB particles, described in Sec. III, is done in a separate step. The resulting, yet undigitized, hits are then overlaid with the physics events under study. Beam-induced background simulation with FLUKA [30, 31] is a resource-intensive process, which usually leads to limited available statistics for the overlay, typically of the order of 10% of a bunch crossing. The available statistics are then increased by adding BIB particle clones with a randomized azimuthal angle.

Previous approaches followed this strategy to prepare a BIB event overlay dataset corresponding to multiple bunch crossings, incurring in significant disk-space usage (a complete BIB event can reach 50 GB on disk) and additional processing times due to the preparation of the overlay datasets, or potentially leading to cross-event correlations if BIB events were used more than once.

In order to minimize the usage of computing resources and ensure the statistical independence of each simulated event, a new overlay algorithm was put in place for this study. It proceeds as follows: the input BIB events are split into fractional pseudo-events; the particles in each pseudo-event are cloned with a randomized azimuthal angle to create an overlay dataset that corresponds to multiple bunch crossings, but kept in separate pseudo-events. The overlay process selects a random combination of pseudo-events to form new BIB events and adds all their particles and detector hits to the physics event. For a large enough number of input pseudo-events, each resulting recombined event for overlay is, to a good approximation, statistically independent from the rest.

The different readout times and resolutions of the different sub-detectors are taken into account by defining integration time windows and selecting hits for the next steps of the simulation. Additional details justifying this procedure are given in Sec. III.

To study the detector performance, we generated samples using single-particle guns comprising either muons, photons, or neutrons. Their angles are distributed uniformly in $0 \leq \phi \leq 2\pi$ and in $8° \leq \theta \leq 172°$ to avoid hitting the beam nozzles directly. Photons and neutrons have a uniform energy distribution and were generated in 4 slices $[0, 50, 250, 1000, 5000]$ GeV, whereas muons have a uniform p_{T} spectrum, divided in 4 slices $[0, 50, 250, 1000, 5000]$ GeV. Each sample is composed of 100,000 events.

III.   EXPERIMENTAL CONDITIONS

Besides the various intrinsic challenges in designing a detector capable of capturing the physics signals occurring in a 10 TeV parton center-of-momentum collider, the muon decays occurring in the proximity of the interaction region contribute an additional source BIB. In the context of this study, we only consider decay-induced background in the detector reconstruction. Other sources of background, such as the beam halo losses [32] in the proximity of the interaction region and the incoherent pair production [33, 34] occurring at the interaction point, are not considered for this study. In particular, the latter could pose a challenge in the innermost tracker elements. The nominal bunch intensity assumed for our simulations is of 1.8×10^{12} muons, with a transverse normalized emittance of 25 µm rad.

The collider lattice[1] under consideration is based on a conventional quadrupole triplet scheme for the final focusing. It consists of a final triplet of quadrupole magnets, immediately followed by the chromaticity correction section, which instead contains dipolar elements. The contribution of the muon decay is relevant only when it happens in the final focusing region, all decays inside the dipole elements produce secondaries which are quickly deflected towards the beam aperture, without reaching the detector area.

To mitigate the background coming from these secondary particles, past studies suggested placing dedicated shielding equipment between the beamline and the detector. In particular, in the context of MAP, they achieved a nozzle-like shape optimized for collider energies up to 1.5 TeV [36, 37]. That conceptual nozzle design contains two main elements surrounding the beryllium beam pipe: an inner tungsten layer to help mitigate the electromagnetic showers and a borated polyethylene cladding to moderate and capture the neutronic component.

―――――――
[1] The collider lattice (tagged with version 0.4) under consideration for this study was developed by past studies during 2022 [35].

The specifics of this element in the latest FLUKA [30, 31] implementation are reported in Figure 1. Starting from that optimized nozzle version, BIB samples for the 10 TeV collider were generated for this study.

Other previous studies had observed a weak dependence of the BIB from the lattice design choices, while the nozzle design appears to have a leading role in the background mitigation [38, 39]. Efforts in optimizing the nozzle for the 10 TeV case are currently ongoing.

This BIB is evaluated with the use of FLUKA Monte Carlo code. The simulation starts from the beam muons decay, sampled from the matched phase-space of the beam. The secondary $e^{+/-}$ produced in the decay are propagated along the collider until they enter the detector area, where the secondary particle propagation is stopped and the relative information stored. Particularly important is the time of crossing in the detector region, since the vast majority of particles are arriving out of time with respect to the bunch crossing.

All particle species except for neutrons are simulated down to 100 keV kinetic energy. This cut is chosen since, below this threshold, the probability of producing a hit in the vertex detector is negligible. Neutrons are transported down to thermal energies. Beyond
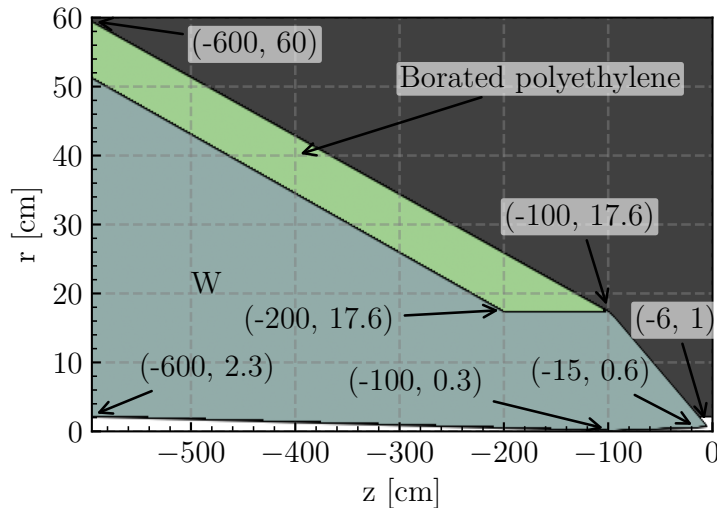

Figure 1: Description of a single nozzle's geometry, with all measurements reported in cm. Both nozzles are cylindrically symmetric symmetry about the z-axis. The green component is borated polyethylene, while the blue-gray area represents pure tungsten (W). The area in black is dedicated to the detector elements, which are not shown.

the default FLUKA physics settings, to enhance accuracy, additional phenomena are enabled such as synchrotron radiation, photo-nuclear interactions, and electro-nuclear interactions.

The various particle spectra are reported in Figure 2. The energy spectrum exemplifies the effectiveness of the nozzle boron layer since the thermal neutron component is completely suppressed. Considering the photon component, the peak in the spectrum contains both the characteristic gamma line in the boron neutron capture (477 keV) and the annihilation peak (511 keV). The impact of the simulated BIB on the detector is shown in Figure 3.

The position where the secondary BIB particles leave the nozzle to enter the detector region plays a dominant role in the background impact. For instance, BIB particles departing from the nozzle in proximity to the tip directly impact the innermost tracker layer, increasing the occupancy.

IV. DETECTOR LAYOUT

The conceptual detector layout is conceived for the highest possible hermiticity given the constraints of the shielding nozzles described above. The BIB mitigation is the primary challenge to approach 4π detector solid-angle coverage. The nozzle extends down to pseudorapidities as low as $|\eta| = 2.44$ (θ values as large as $10°$ with respect to the beam axis). Although the detector can cover the region $|\eta| < 2.44$ without interference with the nozzles, regions of the detector closer to the nozzles will experience additional background. The detector is designed to be approximately azimuthally symmetric with varying n-fold symmetries across the subdetectors. Full azimuthal coverage is assumed.

At the high muon collision energy, the detector must be designed to ensure high-resolution measurements of multi-TeV physics objects. This requires large tracking volumes and deep calorimeters to resolve high-p_{T} particles and minimize punch-through of high-momentum objects. The spatial dimensions and primary materials of each subdetector are described in Table 1.

The geometry of the detector is implemented in the `DD4hep` framework[2] An important limitation of the simulation setup is that passive materials, such as those required for support

---

[2] A "compact" XML format defines the details of the geometry; this structure is translated by `ddsim` to a GEANT4 geometry to inform particle interaction simulation.
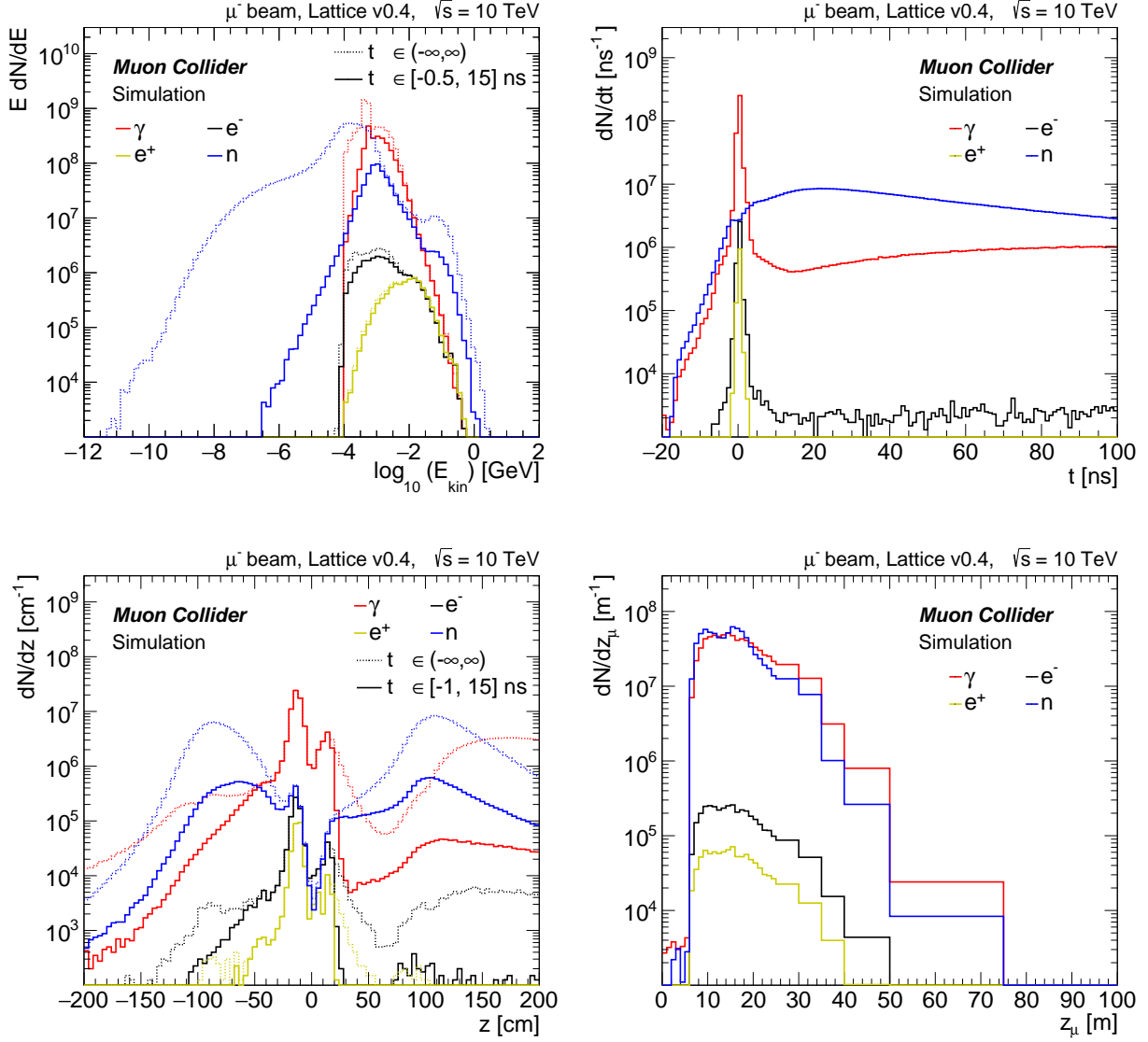
Figure 2: Various spectra of BIB particles as generated by FLUKA are presented. All the results are normalized to the BIB generated during a single bunch crossing at nominal bunch intensity. Only the main particle components are reported (i.e., electrons, positrons, photons, and neutrons). At the top, the energy and time distribution spectra are shown. The bottom-left image displays the distribution of the particle z position at the exit of the nozzle elements, while the bottom-right plot shows the total number of secondary particles as a function of the longitudinal muon decay position: muon decays occurring outside of the final focusing region contribute negligibly to the BIB.
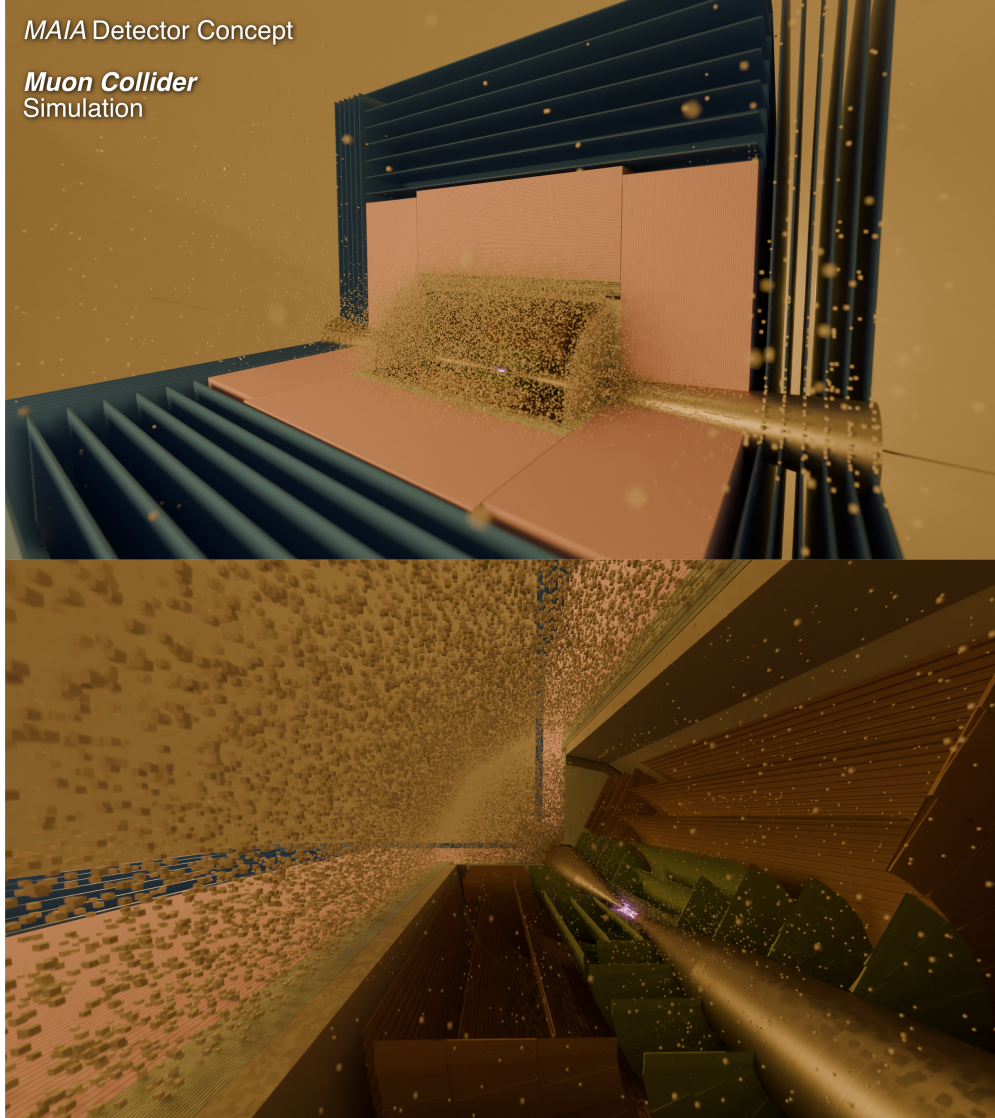
Figure 3: Illustration of a simulated BIB event in the MAIA detector with a cutaway of $\pi/2$ in ϕ. BIB energy depositions in the calorimeters are shown as boxes, and the largest contributions are located in the ECAL and the Vertex Detector.

structures, cryogenics, and cooling, are not present. The beam pipe, nozzles, and high-density solenoid materials are included in the simulation.

An overview of the detector subsystem layout is given in Figure 4. The conceptual design of each subdetector will be discussed in the following sections.

Subsystem	Region	R dimensions [cm]	|Z| dimensions [cm]	Material
Vertex Detector	Barrel	$3.0 - 10.4$	65.0	Si
	Endcap	$2.5 - 11.2$	$8.0 - 28.2$	Si
Inner Tracker	Barrel	$12.7 - 55.4$	$48.2 - 69.2$	Si
	Endcap	$40.5 - 55.5$	$52.4 - 219.0$	Si
Outer Tracker	Barrel	$81.9 - 148.6$	124.9	Si
	Endcap	$61.8 - 143.0$	$131.0 - 219.0$	Si
Solenoid	Barrel	$150.0 - 185.7$	230.7	Al
ECAL	Barrel	$185.7 - 212.5$	230.7	W + Si
	Endcap	$31.0 - 212.5$	$230.7 - 257.5$	W + Si
HCAL	Barrel	$212.5 - 411.3$	257.5	Fe + PS
	Endcap	$30.7 - 411.3$	$257.5 - 456.2$	Fe + PS
Muon Detector	Barrel	$415.0 - 715.0$	456.5	Air + RPC
	Endcap	$44.6 - 715.0$	$456.5 - 602.5$	Air + RPC

Table 1: Boundaries and materials of individual subdetectors.
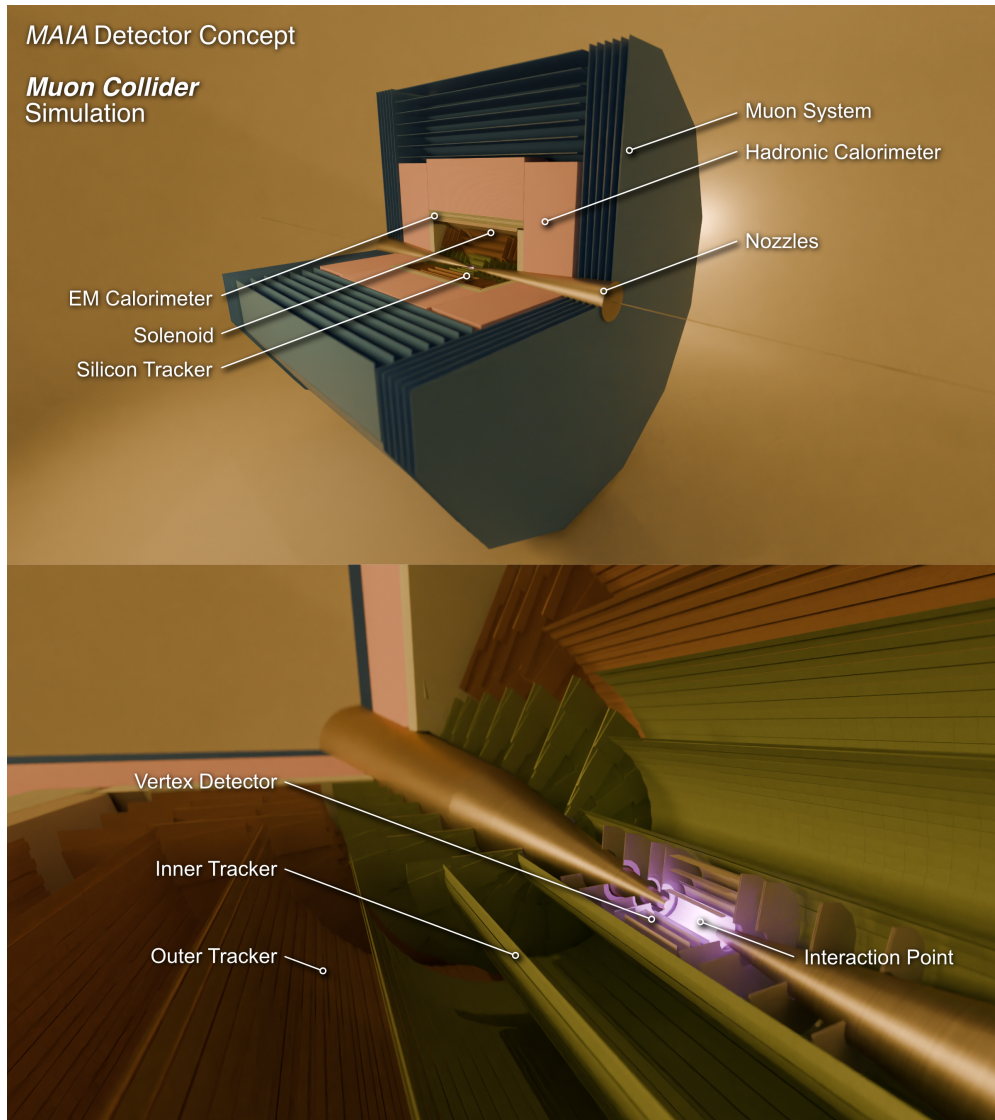
Figure 4: Illustration of the MAIA detector layout, including a closeup of the silicon tracker around the interaction point. The detector is shown with a $\pi/2$ cutaway in ϕ for illustration.

A. Tracking detectors

The reconstruction of charged particle trajectories is a key task for collider experiments. Highly efficient track reconstruction with excellent momentum and impact parameter resolution is imperative to maintain efficiency for reconstructing leptons, jets, energy totals, displaced vertices from heavy flavor hadron decays, and potential new phenomena. The presence of BIB poses significant obstacles to tracking, due to the generation of large data volumes within the tracker and the increase in combinatorial complexity for track reconstruction.

The occupancy and time structure of BIB particles motivate a high granularity detector with precision timing in every layer. The conceptual tracker design comprises three silicon subdetectors summarized in Table 2: the vertex detector, a high-resolution pixel detector closest to the collision point; the inner tracker, a macro-pixel detector; and the outer tracker, a micro-strip detector. The layout and specification of these three sub-systems are based on those of the $\sqrt{s} = 3$ TeV detector design [16], with a few differences detailed below.

In each bunch crossing, BIB particles result in hit densities of up to 1600 hits/cm^2 in the innermost pixel layer. Pixels with $25 \times 25\,\mu\text{m}^2$ granularity and 30 ps resolution timestamps are required to achieve a desired occupancy of 1%. In comparison, the ATLAS and CMS experiments will implement timing detectors with $\sim 1 \times 1\,\text{mm}^2$ pixels and 30 ps resolution

	Vertex Detector	Inner Tracker	Outer Tracker
Sensor type	pixels	macro-pixels	micro-strips
Barrel Layers	4	3	3
Endcap Layers (per side)	4	7	4
Cell Size	$25\,\mu\text{m} \times 25\,\mu\text{m}$	$50\,\mu\text{m} \times 1\,\text{mm}$	$50\,\mu\text{m} \times 10\,\text{mm}$
Sensor Thickness	$50\,\mu\text{m}$	$100\,\mu\text{m}$	$100\,\mu\text{m}$
Time Resolution	30 ps	60 ps	60 ps
Spatial Resolution	$5\,\mu\text{m} \times 5\,\mu\text{m}$	$7\,\mu\text{m} \times 90\,\mu\text{m}$	$7\,\mu\text{m} \times 90\,\mu\text{m}$

Table 2: Spatial and time resolution assumptions for Tracking Detector sub-systems. There is no resolution difference between the barrel and end-cap regions. The first layer of the Vertex barrel and all Vertex endcap layers are implemented as double layers.

based on Low Gain Avalanche Detectors in the outermost layer of the tracker [40, 41]. While there are are several promising sensor technologies for Muon Collider detector needs, the smaller pixel size poses the largest challenge for front-end power consumption and read-out [42]. The detector must also survive an expected 1 MeV neutron equivalent fluence of $1 \times 10^{14-15}$ neq/cm^2 and a total ionizing dose range of 10^{2-5} Gy per year.

The BIB hit density decreases rapidly with radial distance from the beamline, as shown in Figure 5. BIB hits are not uniformly distributed on each tracker plane. Figure 6 illustrates the main dependencies for layers with the highest average occupancy of the vertex detector. The yellow contributions highlight the fraction of hits that are consistent with a window of $[-3\sigma_t, 5\sigma_t]$ with the beam crossing time. This selection almost entirely removes the z
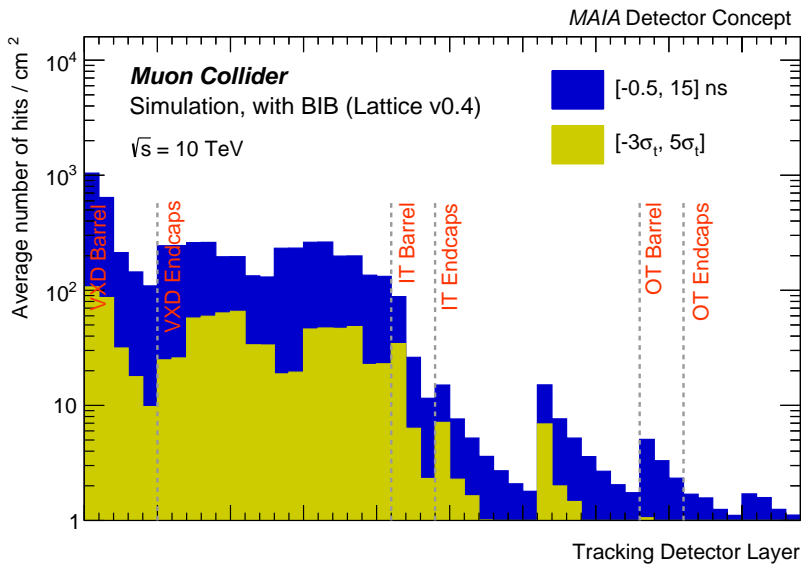
Figure 5: Average hit density in the tracking detectors, shown separately for each detector layer, for $\sqrt{s} = 10$ TeV BIB using the 2023 collider lattice. The yellow histograms include a selection on the hit time, corrected by the time of arrival for particles traveling at the speed of light. The selection applies a window of $[-3\sigma_t, 5\sigma_t]$ from the beam crossing, where σ_t refers to the detector time resolution. The dashed lines highlight the boundaries between sub-detectors and the orange text specifies the sub-detector name. The bins are ordered respectively by ascending radius for barrel detector and ascending $|z|$ for endcap detectors, with $z < 0$ layers preceding those with $z > 0$.
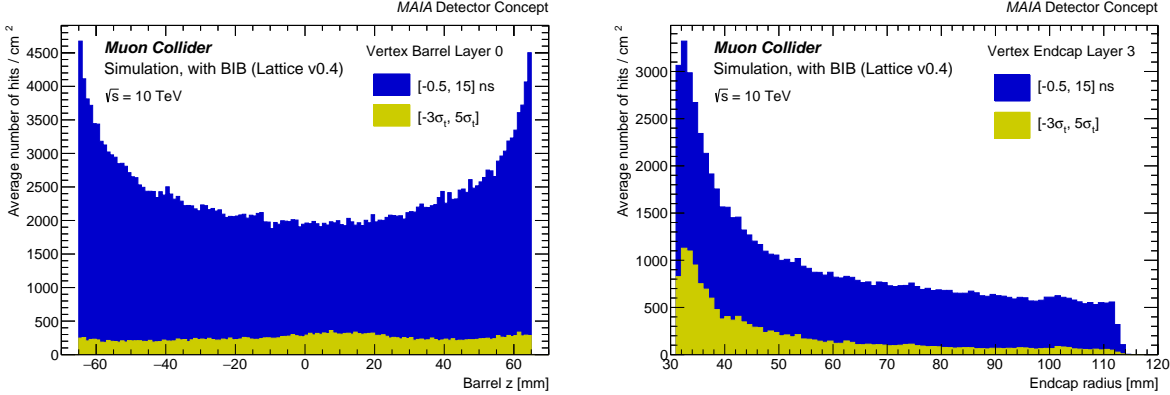
Figure 6: Hit density in highest average occupancy layers the Vertex detector barrel (left) and endcap (right). Densities are shown as a function of the longitudinal or radial position, for $\sqrt{s} = 10$ TeV BIB.

dependence in the barrel region, with limited mitigation on the radial dependence in the endcap disks.

When operating at $\sqrt{s} = 10$ TeV, background from incoherent production of e^+e^- pairs is expected to become sizeable. A simulation of this background is not currently included, and will be addressed in future work. This additional flux of particles is expected to populate the forward region of the first few layers of the vertex tracker, possibly tightening the requirements on the detector technology that will need to be deployed in those regions.

The tracking system is embedded in a 5T solenoidal magnetic field, in contrast to the 3.57T solenoid of the 3 TeV detector design. The increased magnetic field maintains precision momentum resolution for the highest momentum charged particles produced in collisions. The higher field also reduces the radius of curvature for low momentum particles, resulting in reduced occupancy with respect to $\sqrt{s} = 3$ TeV.

Another notable difference with respect to the 3 TeV design is the reduction in doublet layers in the Vertex Detector. Doublet layers are used to reduce the computational complexity of track reconstruction by requiring that pairs of hits are consistent with a particle produced at the interaction point. For the 3 TeV design, all Vertex layers were implemented as doublet layers. The 3 TeV design assumed Conformal Tracking, optimized for the clean environment of e^+e^- colliders, and required doublet layers to reduce the time needed to reconstruct an event. A Combinatorial Kalman Filter, developed for the busy environment

of hadron colliders, is now used and can perform track reconstruction in a reasonable time without requiring any additional filtering of input hits. Doublet layers in the outer three layers of the Vertex Detector are no longer necessary due to these improvements.

B. Calorimetry

Compared to the tracker, the calorimeter has some advantages in BIB resilience: it has a higher radius, resulting in a lower flux, and its energy-proportional response means that high-energy signatures can be picked out with relative ease. However, the larger cell sizes and longer integration times associated with most calorimeter technology mean that BIB can still degrade performance.

The MAIA detector concept makes use of a silicon-tungsten electromagnetic calorimeter (ECAL) and an iron-scintillator hadronic calorimeter (HCAL). Both systems are based on the CLIC calorimeter design [43], which was also the starting point for earlier iterations of a muon collider detector optimized for $\sqrt{s} = 3$ TeV [16]. Compared to the calorimeters optimized for lower energy, this detector concept has more layers, and each layer has a slightly thicker absorber. The cells have also been slightly scaled up in size. More detail can be found in Table 3.

The design of the calorimetry for this detector is a modest extension of current technology. The technical specifications of the ECAL's silicon are similar to that of the CMS high granularity calorimeter (HGCAL), currently under construction for the High-Luminosity LHC upgrade [44]. The cell sizes are slightly smaller in the MAIA design, and the sensors

	Electromagnetic Calorimeter	Hadron Calorimeter
Cell type	Silicon - Tungsten	Iron - Scintillator
Cell Size	$5.1\,\mathrm{mm} \times 5.1\,\mathrm{mm}$	$30.0\,\mathrm{mm} \times 30.0\,\mathrm{mm}$
Sensor Thickness	$0.5\,\mathrm{mm}$	$3.0\,\mathrm{mm}$
Absorber Thickness	$2.2\,\mathrm{mm}$	$20.0\,\mathrm{mm}$
Number of layers	50	75

Table 3: Cell and absorber sizes in the calorimeter systems, describing both the barrel and end-cap regions.

are slightly thicker, but the overall parameters are similar. The HGCAL will have a 50 ps timing precision. The MAIA HCAL is similar in design to the ATLAS Tile Calorimeter, albeit with smaller cells by roughly a factor of 10 in each direction [45], and a timing resolution is roughly 1 ns. MAIA's ECAL and HCAL simulations have not yet assumed similar timing resolution to their LHC equivalents, but instead currently sum all deposits made from -0.5 to 10 ns with respect to the expected time of arrival.

The largest change in the MAIA detector relative to the 3 TeV detector is the relocation of the solenoid just outside of the tracker. The presence of the solenoid material in front of the electromagnetic calorimeter reduces the incoming BIB particle flux. The solenoid adds approximately 265 mm of aluminum and thinner steel layers in the region $|z| \lesssim 2.3$ m, and additional steel layers in the endcap region. Figure 7 shows the energy density per layer comparing the proposed layout with the 3 TeV detector design. The presence of the additional material, equivalent to approximately 4 X_0 and 1 λ for a particle crossing the material in the transverse direction, reduces the incoming BIB flux by a factor of 10. Of course, this shielding also impacts the incoming signal, but it is possible to perform calibrations (discussed in Sec. V) that mitigate much of this impact.
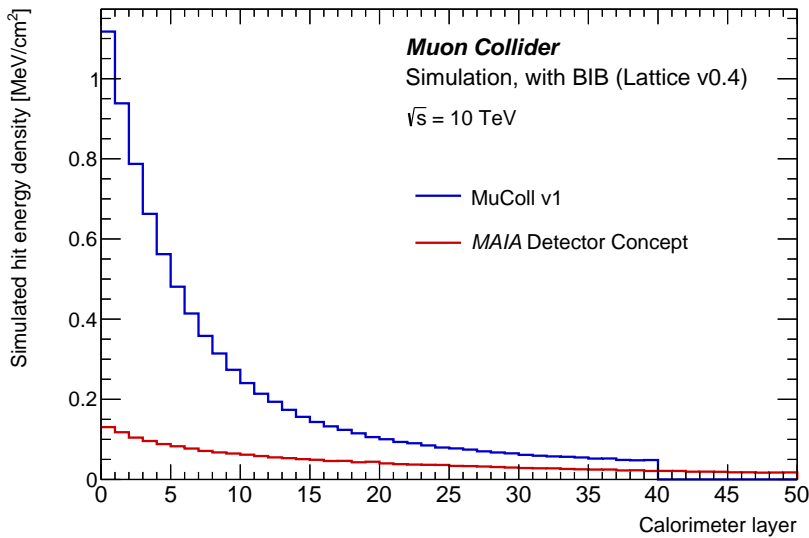
Figure 7: Average energy density of simulated BIB hits for each ECAL barrel layer. The layer index increases with radius. The same BIB particles are propagated through the 3 TeV detector (MuColl v1) and the MAIA concept to illustrate the effects of the solenoid placing.

The BIB particles that reach the calorimeters are mostly photons and neutrons. Figure 8 illustrates the BIB energy spectrum for two ECAL cells placed in the barrel and endcap regions. The timing and spatial distribution of the BIB are both highly diffused. In this study, BIB hits in the timing window from -0.5 to 15 ns (relative to expected time of arrival for particles coming from the interaction point) are included in the digitization process, and no further assumptions are made about timing.

BIB particles are predominantly very low energy, but their extremely large multiplicity creates a significant diffuse signal in the calorimeter. For reconstruction algorithms that focus on very localized depositions, like the photon reconstruction algorithm employed here,
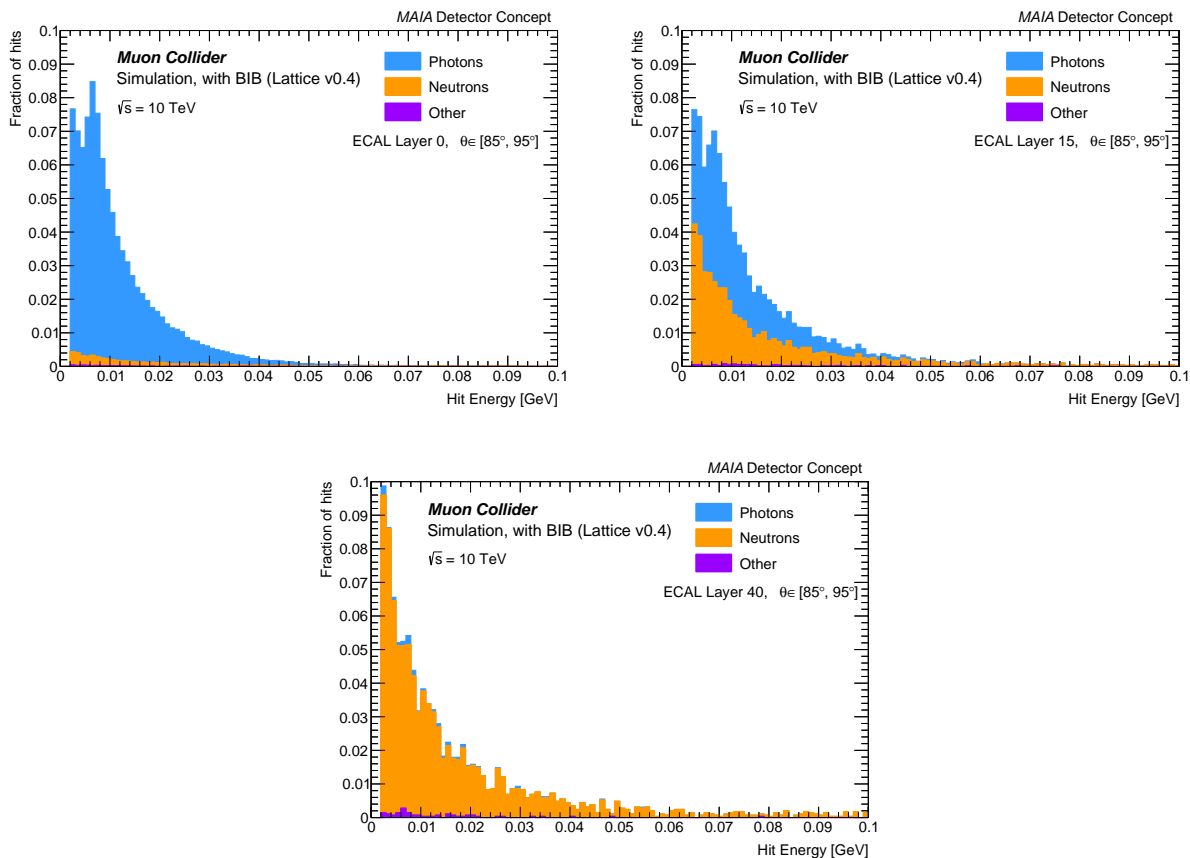
Figure 8: Composition of the average BIB hit energy spectrum in selected ECAL regions, for different layers of the calorimeter. The colored components highlight the type of particle that originated the shower in the calorimeter cell. The shallower layers are dominated by photon energy deposits, while the deeper layers are dominated by neutrons. The contribution marked as "Other" includes muons and other hadrons.

pure BIB depositions rarely create clusters energetic enough to fake a reconstructed particle. With out-of-the box photon reconstruction (developed for e^+e^- environments) and no identification criteria applied, typical events have less than five fake photons with energies above 20 GeV. However, this BIB contribution can still negatively affect true reconstructed photons, adding energy to the clusters and shifting their centroids. Dedicated algorithms, which employ cleaning methods and more detailed timing information, could provide substantial improvement in both the resolution and fake rate of these algorithms.

In this study, variable cell thresholds are introduced in order to mitigate the effects of BIB particles. The thresholds vary as a function of the polar angle θ and the calorimeter layer. In the central part of the calorimeter, the diffused BIB photon component becomes negligible and the thresholds can be lowered to target the leftover energy deposition from neutrons. Each cell is also corrected by subtracting the statistical mode of the expected BIB contribution in that region of the detector. The application of these variable thresholds further reduces the BIB contribution by an average of 65%.
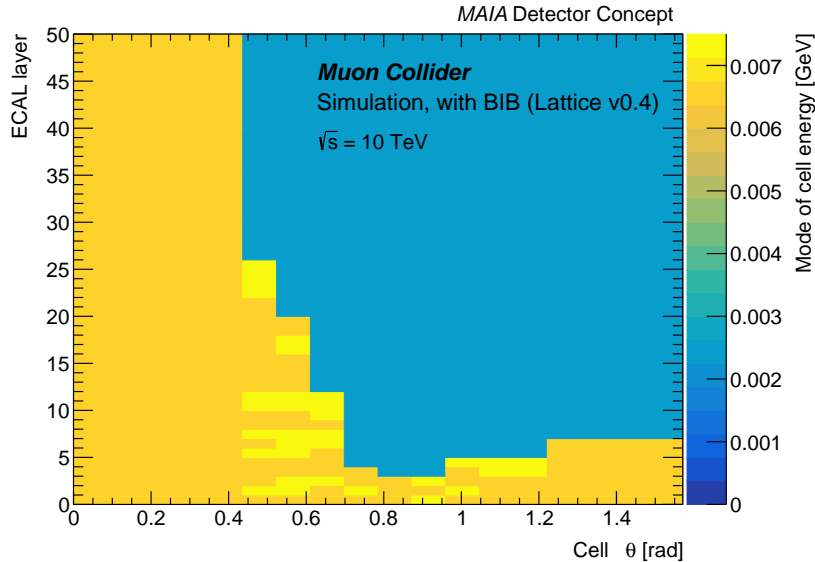
Figure 9: Mode of ECAL cell energy as a function of theta and calorimeter layer.

C. Muon system

Muon systems are expected to be the least affected by the presence of BIB. A notable exception to this statement is the forward regions at very small angle [16], where the muon detectors are reached by particles exiting the absorbing nozzles.

In the MAIA design, the lack of a magnetic field relegates the muon system to the role of particle identification. This is achieved by reconstructing straight track segments matched to extrapolated inner tracker trajectories.

The layout and baseline technology of the muon system are kept the same as used in the 3 TeV detector presented in Ref. [16], although with increased dimensions to fit the volume of the other subsystems. The expected detector occupancy and track-finding performance were found compatible with those described in Ref. [16]. No matching with the tracking detector tracks was put in place yet, but it was assumed that the muon system design should deliver adequate particle identification performance.

V. DETECTOR PERFORMANCE

The performance of the proposed detector was studied using the single particle gun samples described in Section II. The performances of the tracker, ECAL, and HCAL were evaluated in terms of reconstruction efficiencies and resolutions on their measurement targets: tracks, photons, and neutral hadrons, respectively. By focusing on neutral particles, calorimeter performance can be evaluated with minimal dependence on particle flow for matching tracks to calorimeter cell clusters, as these and other high-level reconstruction algorithms remain in need of optimization.

Studies are performed with and without BIB overlay. For reference, where relevant, the performance of the 3 TeV detector layout described in Ref. [16] in the presence of 10 TeV BIB is also discussed.

A. Tracks

As described in Section II, track reconstruction is performed using a Combinatorial Kalman Filter developed for the high occupancy environment of hadron colliders, which is also reasonably well suited to the large BIB present at a muon collider. To mitigate the

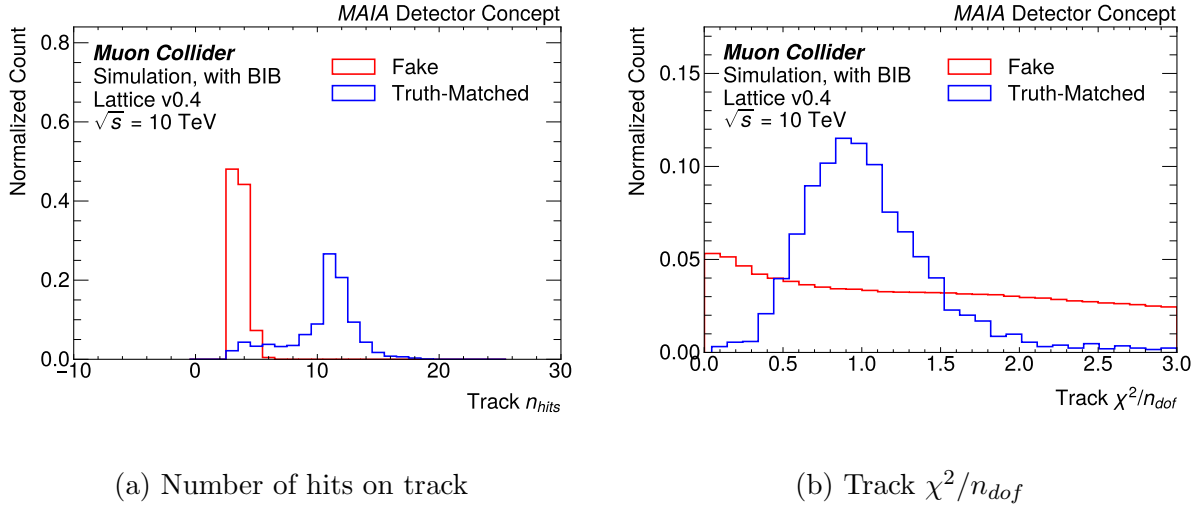(a) Number of hits on track (b) Track χ^2/n_{dof}

Figure 10: Track parameter distributions with BIB overlaid comparing truth-matched tracks to falsely reconstructed tracks.

impact of BIB, hits considered for track reconstruction are required to be consistent with particles produced at the collision. Hit times, corrected by the time-of-flight for a particle traveling at the speed of light, are required to be within a window of $[-3\sigma_t, 5\sigma_t]$ from the beam crossing, where σ_t refers to the detector time resolution.

Track reconstruction performance is studied with single muon samples, where all muons are produced at the origin, with and without BIB overlaid. Hits from BIB pose a challenge for pattern recognition and can result in a large rate of *fake tracks* reconstructed from random combinations of hits. The properties of these fake tracks are compared to those of real, correctly reconstructed muon tracks in Figure 10. Roughly half of fake tracks from BIB have $p_{\mathrm{T}} < 1$ GeV, and nearly all have large d_0 and ≤ 5 hits on track. To select prompt tracks of interest for subsequent analysis and reduce the rate of fake tracks, we apply *track cleaning* requirements of $p_{\mathrm{T}} > 1$ GeV, $|d_0| < 0.1$ mm, $n_{\mathrm{hits}} \geq 5$ and $\chi^2/n_{dof} < 3$. A study of displaced track reconstruction performance is left for future work.

The track reconstruction efficiency degrades in the presence of BIB, as shown in Figure 11. With BIB overlaid, the total efficiency to reconstruct a track is 86%, reduced to 80% after track cleaning. Without BIB, the total efficiency is 96%, reduced to 94% after track cleaning. Figure 12 and Figure 13 also show the efficiency as a function of track transverse momentum for the barrel and endcap regions, respectively. Without BIB, track reconstruction in the

barrel region ($40°<\theta<140°$) is 99.6% efficient, compared to the endcaps which have an efficiency of 89.7%. When BIB is included these efficiencies degrade to 96.3% for the barrel and 70.5% for the endcap. These results are expected due to the geometry of the tracker, which is optimized for the barrel region. An optimization of the endcap geometry, especially in the presence of BIB, is left for future work.
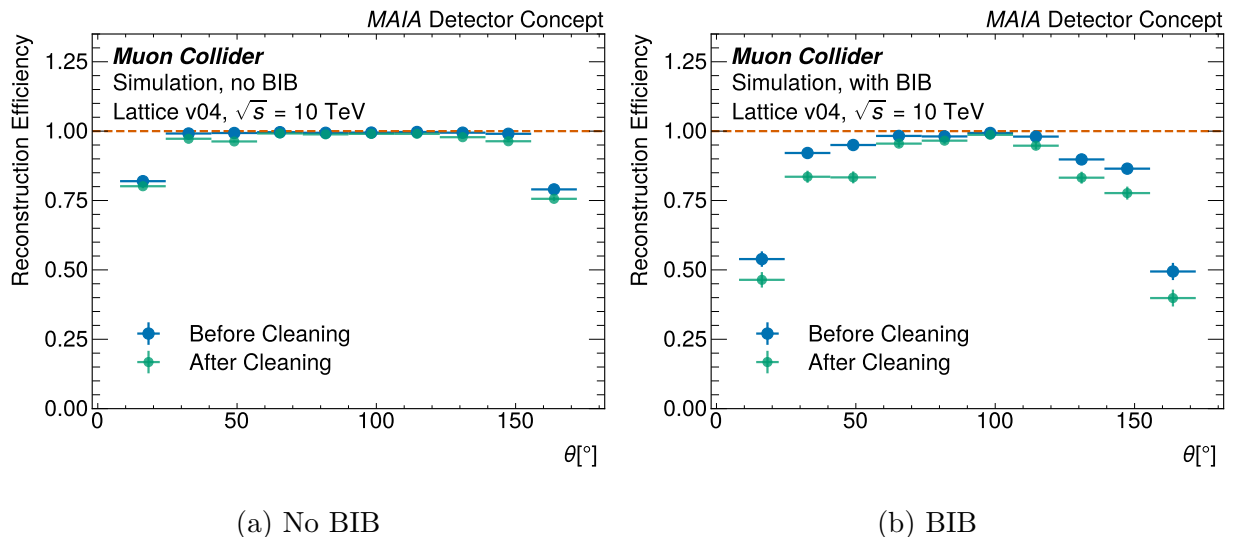

(a) No BIB

(b) BIB

Figure 11: Track reconstruction efficiency as a function of θ comparing tracks before and after cleaning.

(a) No BIB, Barrel Region
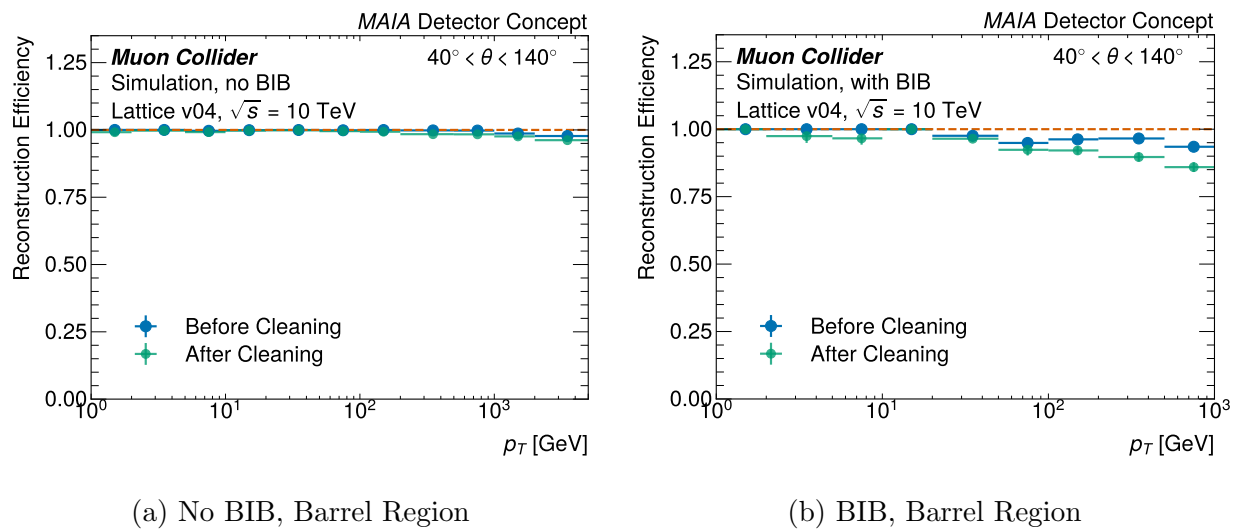
(b) BIB, Barrel Region

Figure 12: Track reconstruction efficiency in the barrel region as a function of p_T comparing tracks before and after cleaning.
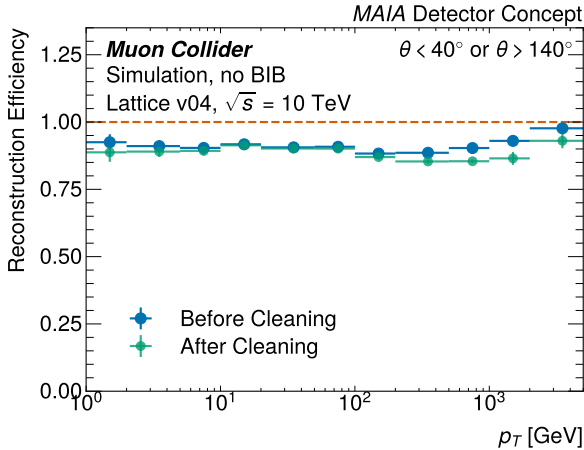
(a) No BIB, Endcap Region   (b) BIB, Endcap Region
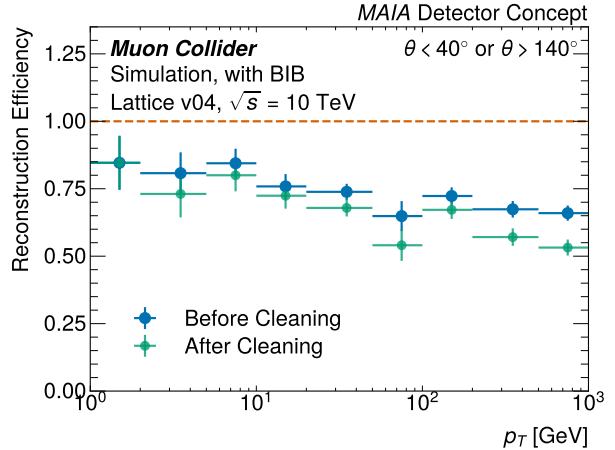
Figure 13: Track reconstruction efficiency in the endcap region as a function of p_T comparing tracks before and after cleaning.

Figure 14 and Figure 15 show the transverse momentum and transverse impact parameter resolution for tracks which pass cleaning requirements, respectively. The transverse momentum resolution is computed by comparing reconstructed and generated p_T. Momentum resolution ranges between a few percent for the lowest p_T sample in the barrel and 10% for the highest momentum sample. The transverse impact parameter resolution is computed by comparing reconstructed and generated d_0. The resulting impact parameter resolution is found to be consistently below 10 μm, and is unaffected by the presence of BIB.

B. Photons

Photon reconstruction relies primarily on the high-granularity measurements made in the Electromagnetic Calorimeter (ECAL). In this study, the ECAL showers resulting from a photon gun are simulated using GEANT4, and digitized using a process that smears simulated energy deposits according to Poisson fluctuations. All hits in a given cell with timing (corrected for propagation time from the interaction point) from -0.5 to 10 ns are summed into a single output. No further timing information is used in the reconstruction used in this study, though significant BIB reduction could be achieved through tighter and more nuanced timing cuts. After this process, a threshold of 0.05 MeV is applied to each cell, and a maximum cell energy deposit of 2.36 GeV is enforced. This upper threshold
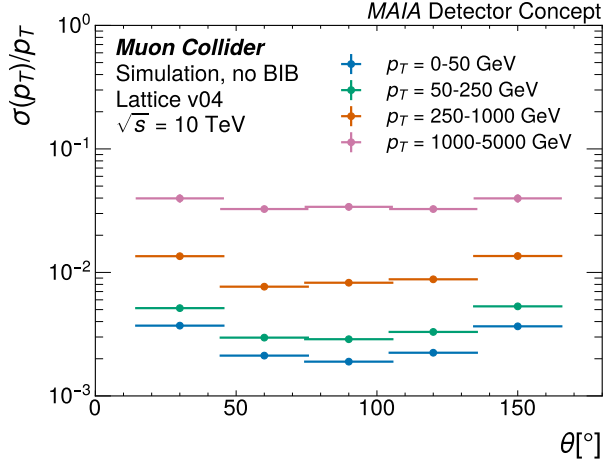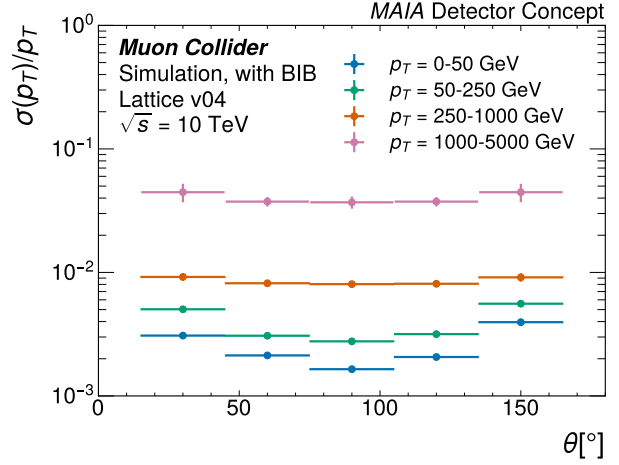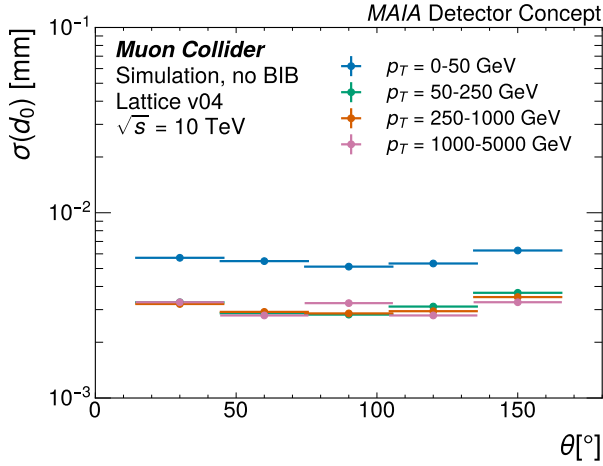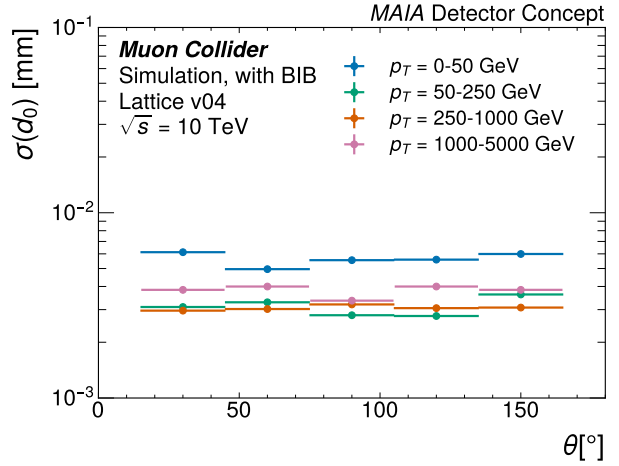
(a) No BIB   (b) BIB

Figure 14: Track p_T resolution as a function of θ comparing four p_T ranges of 0-50 GeV, 50-250 GeV, 250-1000 GeV, and 1-5 TeV.

(a) No BIB   (b) BIB

Figure 15: Track d_0 resolution as a function of θ comparing four p_T ranges of 0-50 GeV, 50-250 GeV, 250-1000 GeV, and 1-5 TeV.

was arbitrarily chosen to be sufficiently high its impact was not discernible. In the case of samples with BIB overlay, this minimum threshold is superseded by the much higher region-specific thresholds shown in Fig. 9. An event display of a single photon gun sample overlaid with BIB is shown in Figure 16.
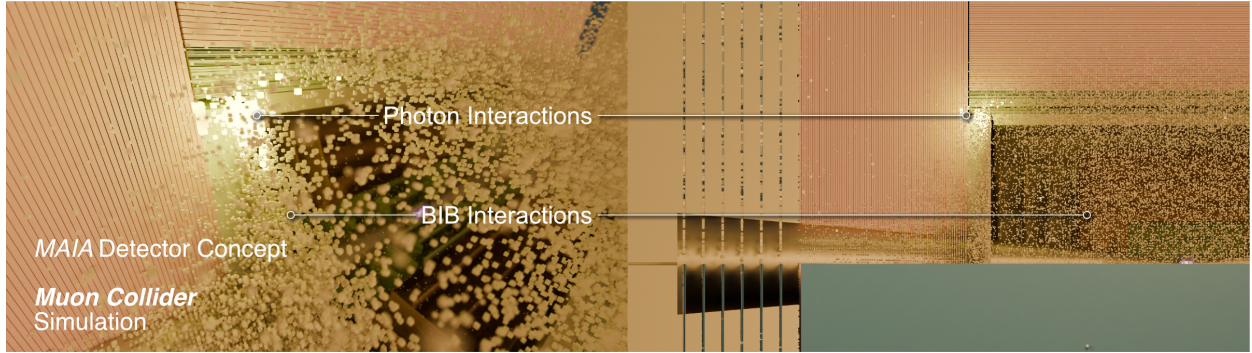
Figure 16: As simulated in GEANT4, detector hits from the shower of a photon with an energy of 62 GeV are shown in yellow along with hits from BIB. A 3D perspective view (left) and an orthographic $R - z$ projection (right) are shown.

Photons are reconstructed using the Pandora particle flow algorithm, which uses an initial cone-clustering algorithm, followed by a series of re-clustering steps to form cluster candidates [46]. Electromagnetic and hadronic showers are differentiated via a series of topological requirements. Photons are differentiated from electrons via the presence of an associated track. This algorithm is not optimized for a muon collider environment, and future work will investigate how to make the clustering more robust to contributions from BIB.

Studies of the algorithm were performed using a photon gun with and without BIB overlay. Objects identified as photons by Pandora were matched to true photons if they were within $\Delta R < 0.1$ of the true photon and had a reconstructed energy > 20 GeV. If multiple photon candidates satisfied that requirement, the one with highest energy was selected as the match. Our reconstructed energy threshold was chosen in order to exclude a larger fraction of BIB particles and address difficulties in matching; lower thresholds led to frequent mismatching. We therefore only study photons with true energy ≥ 30 GeV. The efficiency of the algorithm is shown in Fig. 17. For photons with energy greater than 100 GeV, the efficiency is high, hovering around 95%. Below that value, the efficiency drops slightly, decreasing to around 90% for a 30 GeV photon.

To study energy resolution, a response function was determined from simulation without BIB, simultaneously binned in reconstructed photon energy and θ. This response function, shown in Fig. 18a, had the largest deviations from unity for photons with low energy in the transition regions (between forward (endcap) and barrel regions). These photons are

26

most impacted by the additional material introduced with the relocation of the solenoid, and this response function serves to scale up their energies to correct for this effect. The resolution is somewhat worsened in these regions, as shown in Fig. 18b for electrons with energy ≥ 600 GeV. The effect is most dominant in the high energy regime where the nominal resolution is small.
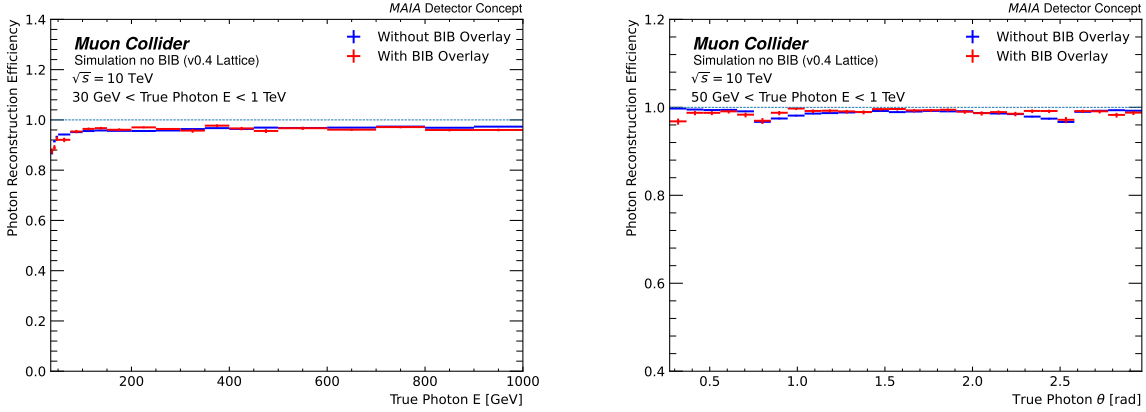
(a) Photon efficiency vs true energy

(b) Photon efficiency vs true theta, with low-energy photons suppressed

Figure 17: Photon reconstruction efficiency with BIB overlay. True photons are matched to the highest energy and lowest ΔR photon candidate within $\Delta R \leq 0.1$.
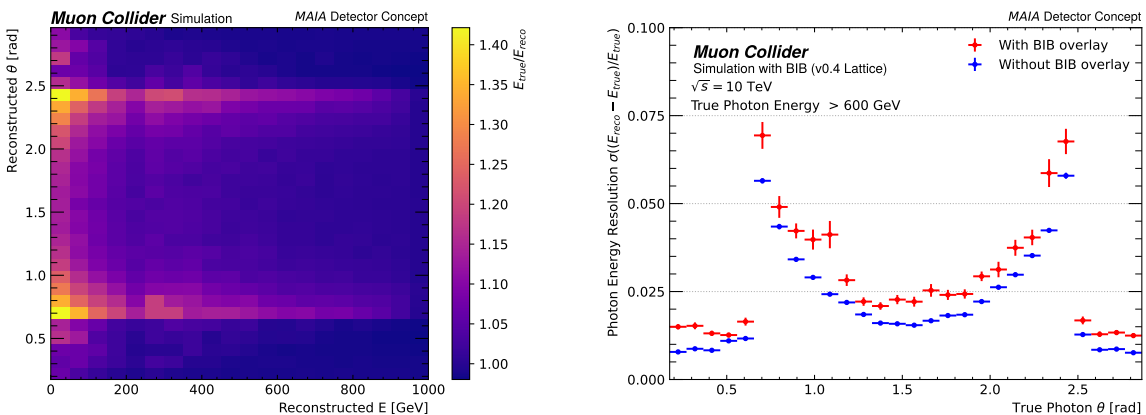

(a)

(b)

Figure 18: (a) Measured simulated energy response in θ and E (no BIB overlay). Response histogram used to calibrate reconstructed photon energy. (b) Photon energy resolution plotted against θ for photons with $E \geq 600$ GeV.

The resolutions as a function of energy in the different regions can be seen in Fig. 19. It is clear that photons in the endcap region (no solenoid material present) are better resolved than those in the transition and barrel regions. The energy loss in these latter regions depends both on how many radiation lengths the particle traverses in the magnet and how deep into the magnet the particle begins to shower (a stochastic process that is non-trivial to model). Therefore, a scaling response function alone cannot prevent some random broadening of the resolution in the regions where particles interact significantly with the solenoid. In addition to more advanced BIB rejection strategies, a detailed study of stochastic energy loss may mitigate the degraded resolution.
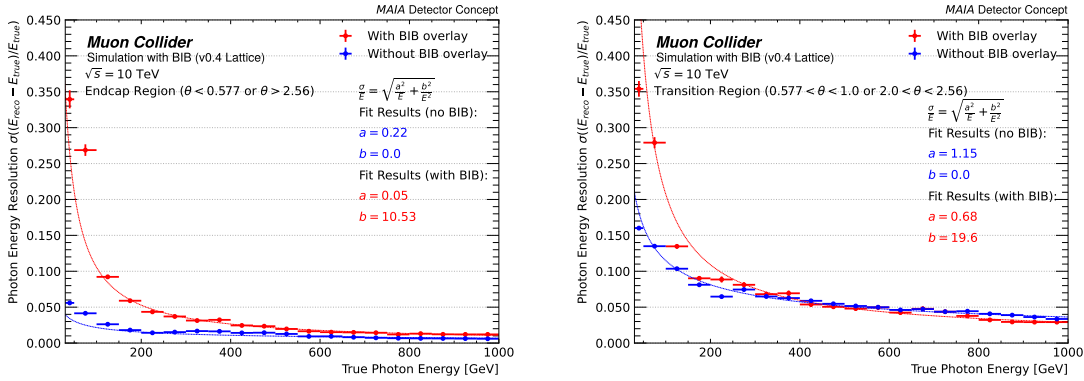
(a) Photon energy resolution, endcap region

(b) Transition region
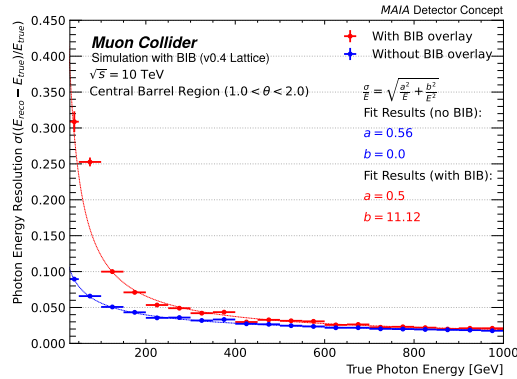
(c) Barrel region

Figure 19: Photon energy resolution of reconstructed photons vs true photon energy, split into the three regions by theta. The performance in the transition region suffers slightly more than the other regions due to the presence of the solenoid.

28

C. Neutral hadrons

Neutral hadron reconstruction relies primarily on the Hadronic Calorimeter (HCAL). The characterization of the HCAL performance is accomplished by studying the reconstruction efficiency and energy resolution of neutron showers simulated with GEANT4, with the same cell timing and energy threshold requirements as described for the ECAL in Section V B. In Fig. 20, a 73 GeV neutron shower event display shows neutron cell hits in green and BIB hits in brown.

Neutrons are reconstructed using Pandora's particle flow algorithm for samples with and without BIB overlays [46]. From this reconstruction, Pandora creates particle flow objects (PFOs), which are candidates for the generator neutron. Since Pandora clustering is not optimized for a muon collider environment, soft clusters are highly contaminated with BIB energy and cannot be discerned from the BIB background. Therefore, PFOs with $E_{PFO} < 20$ GeV are rejected, and all studies require a cut of 30 GeV on the truth energy, E_{true}. The E_{true} cut limits the low-energy biasing created by a PFO energy cut. Since this study uses high-energy neutron guns, there is a high probability that reconstructed neutron showers are split into multiple PFOs by the time they reach the calorimeter. To properly capture the reconstructed energy, E_{reco} is the summed energy of all PFOs satisfying $E_{PFO} > 20$ GeV within a ΔR cone of 0.1. The PFO energy is summed regardless of particle ID, but final PFO matching requires at least one PFO neutron within the $\Delta R = 0.1$ cone.
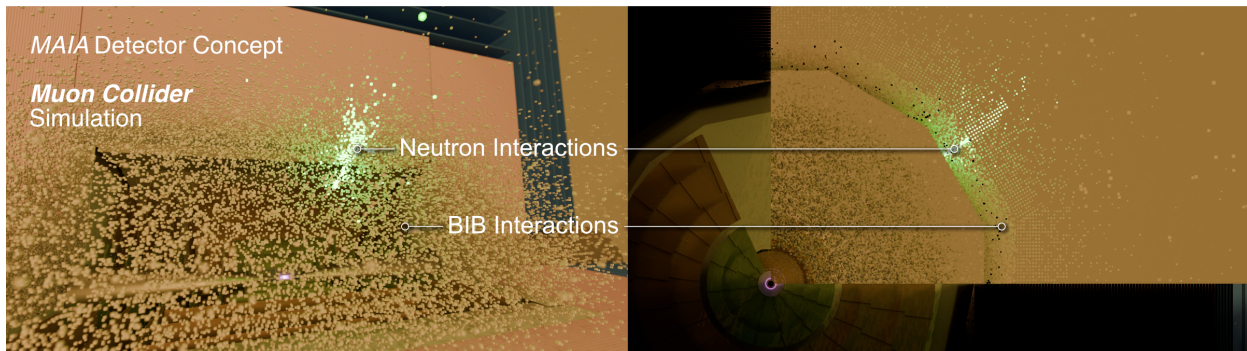

Figure 20: As simulated in GEANT4, detector hits from the shower of a neutron with an energy of 73 GeV are shown in green along with hits from BIB. A 3D perspective view (left) and an orthographic $x - y$ projection (right) are shown.

The efficiency of PFO matching with Pandora's reconstruction algorithm is shown in Figs. 21 and 22. Fig. 21a shows the reconstruction efficiency across E_{true} in the central barrel region ($1.0 < \theta_{true} < 2.0$). As expected, the efficiency is best in the central barrel region, with efficiencies $> 90\%$ for neutrons with $E_{true} > 100$ GeV. In this region, the efficiency is similar between samples with and without the BIB overlay across all energies. In Fig. 21b, the efficiency plot inclusive in θ plateaus around 85% compared to 95% for the barrel region suggesting that the efficiency in the endcaps and transition regions is lower than in the barrel. The angular dependence on reconstruction efficiency across all θ is shown in Fig. 22. Fig. 22a shows the reconstruction efficiency for high-energy neutrons with $E_{true} \geq 250$ GeV, and Fig. 22a is for $E_{true} < 250$ GeV. The discrepancy in efficiency between the two energy batches is described by the previous plots over energy. The efficiency, however, does show a significant dependence on θ. Looking at the high-energy batch, the efficiency drops significantly from 95% in the barrel to 80% both in the transition regions ($0.577 < \theta_{true} < 1.0$ and $2.0 < \theta_{true} < 2.565$) and below 60% as θ approaches the nozzles. Improving the efficiency in the endcaps is also an area of future work. The drop in efficiency for forward neutrons is the primary contributor to the loss of efficiency in the inclusive region efficiency plot compared with the central barrel region (Fig. 21.) Also, in the transition
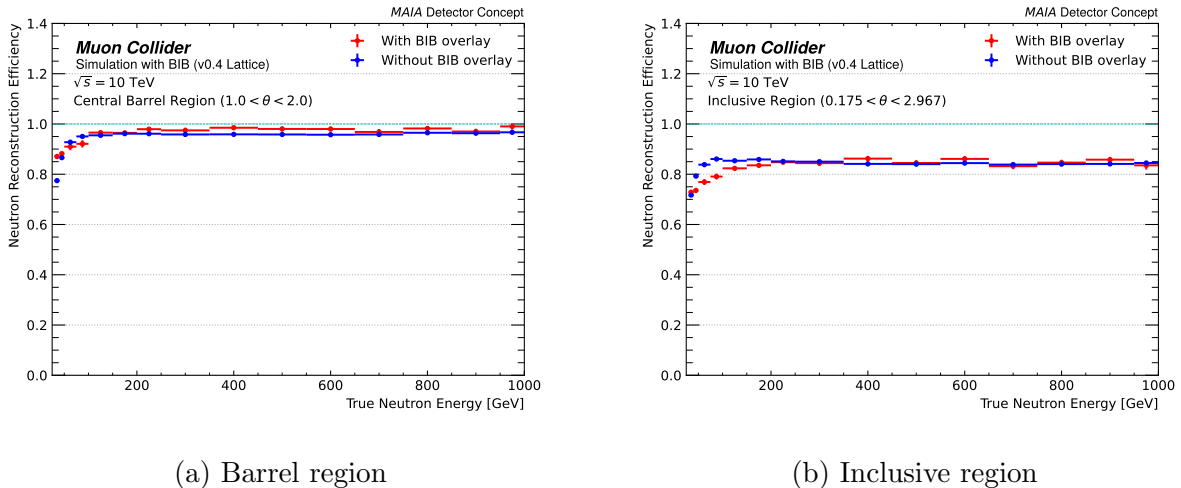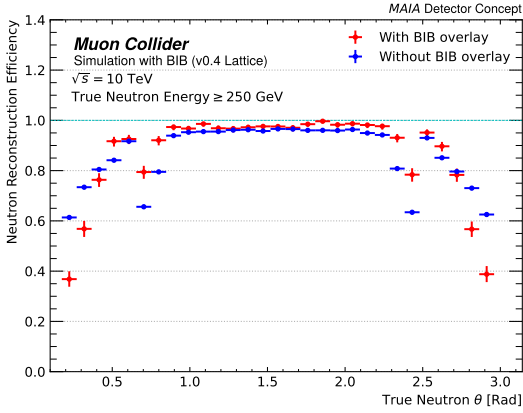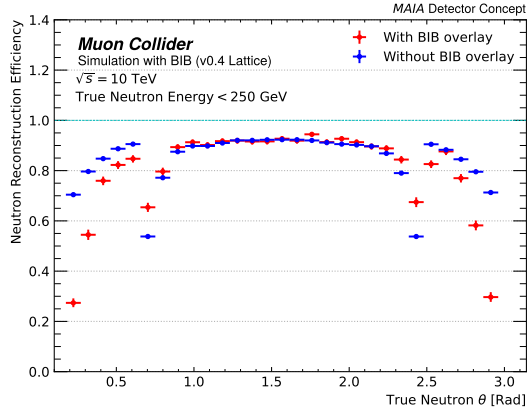

(a) Barrel region   (b) Inclusive region

Figure 21: Neutron reconstruction efficiency vs E_{true}. These plots are split into the barrel region of the detector as well as the inclusive region which includes the barrel, endcap, and transition regions.

(a) $E_{true} \geq 250$ GeV (b) $E_{true} < 250$ GeV

Figure 22: Neutron reconstruction efficiency vs θ_{true}. These plot sare split into two batches with $E_{true} \geq 250$ and $E_{true} < 250$.

regions, the samples with the BIB overlay have greater efficiencies than those without BIB. This suggests BIB contamination in the PFOs from this region generating fake reconstructed neutrons. This issue will hopefully be improved by adapting the reconstruction to a muon collider environment in the future.

In studying the energy resolution, a response function like the one used in the ECAL is not used. This is because the energy response of neutrons with $E_{true} > 30$ GeV is within 5% across all E and θ for samples without the BIB overlay, except for a 7.5% dip in the transition regions. Since the solenoid material is fewer interaction lengths for neutrons than photons, the HCAL is less impacted by the move of the solenoid than the ECAL is. However, for samples with the BIB overlay, low-energy neutrons have a large positive response due to BIB energy contamination, while high-energy neutrons have a roughly 20% energy loss.
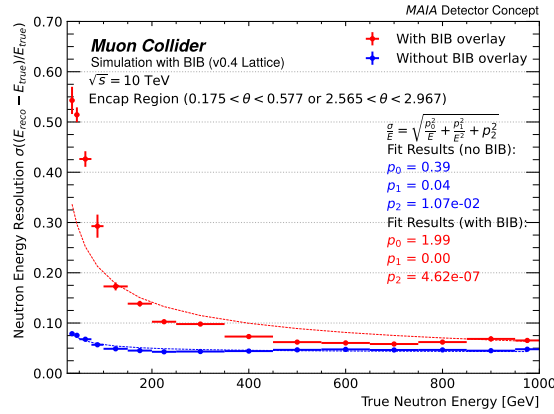
The reconstructed neutron energy resolution, $\sigma_E = \sigma\left(\frac{E_{reco} - E_{true}}{E_{true}}\right)$, is shown in Figs. 23 and 24. Fig. 23 is split into the barrel, transition, and endcap regions. In all regions, σ_E plateaus around 6% for neutrons without the BIB overlay. The addition of BIB moderately degrades the resolution to below 15% or $E_{true} > 200$ GeV in the central barrel where the resolution is best. Still, σ_E across all three regions is within the $35\%/\sqrt{E}$ initial goal set for HCAL performance for neutrons with the BIB overlay. The resolution will also likely be improved by more refined reconstruction methods.
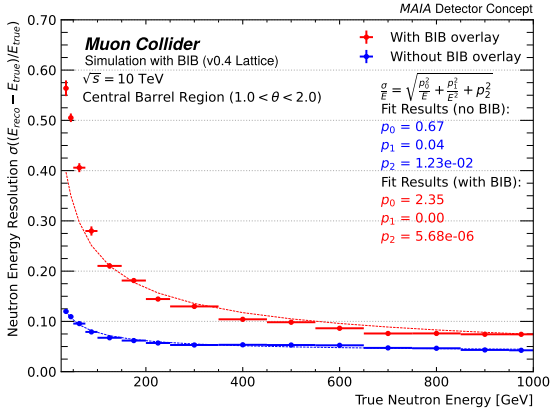
(a) Barrel region
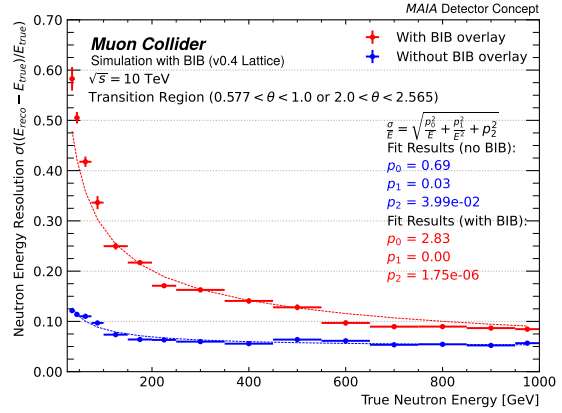
(b) Transition region

(c) Endcap region

Figure 23: Reconstructed neutron energy resolution over true neutron E. These plots are split into the barrel region of the detector as well as the inclusive region which includes the barrel, endcap, and transition regions.

The θ dependence on σ_E is shown in Fig. 24 which is split into the same batches as the efficiency plots. For samples without the BIB overlay, the resolution is similar for the barrel and endcaps. There is a spike in the transition region, however, which is expected from the shape of the solenoid. Looking at the BIB overlay samples, the resolution is worse overall with a similar shape to the samples without BIB. For high-energy neutrons, the θ dependence only varies by less than 5% across the detector.
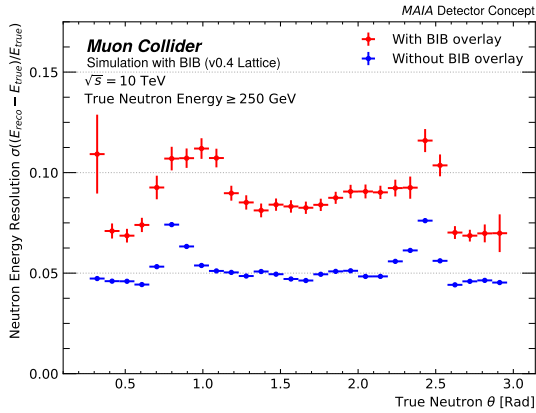
(a) $E_{true} \geq 250$ GeV
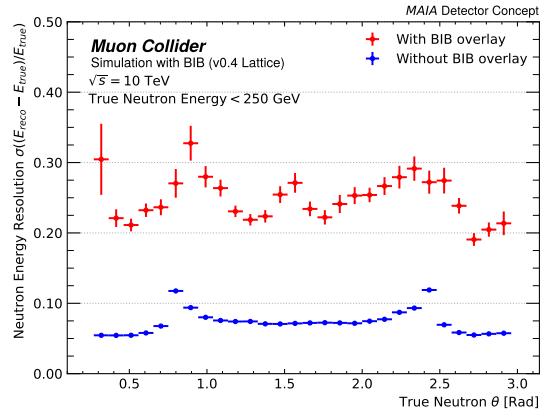
(b) $E_{true} < 250$ GeV

Figure 24: Reconstructed neutron energy resolution as a function of true neutron θ. These plots are split into two batches with $E_{true} \geq 250$ and $E_{true} < 250$.

VI. FUTURE WORK

This conceptual detector design can be used for further study, particularly for higher-level object reconstruction and physics projections in the presence of beam-induced and SM collision backgrounds. The performance of this detector is expected to increase with further optimization of the detector geometry, subdetector technology choice, and reconstruction algorithms. As the details of the accelerator lattice, particularly the final focus and length of the straight sections leading to the experimental area, change, the character and level of the BIB is expected to change. Such changes may require additional reoptimization of the detector design as needed.

The optimization of the nozzle geometry, material, and structure remains a major area for improvement. Small changes to the geometry or material makeup of the nozzle can have significant effects on occupancy of the detectors, particularly for the region closest to the collision. Coarse optimizations have been performed. However, running BIB simulation through iterative nozzle designs is computationally intensive, and major improvements in computing may be crucial in efficiently exploring the full space of nozzle designs. The use of machine learning, such as generative networks to more efficiently simulate interactions with the nozzle [47], may be valuable in this optimization.

We plan to explore major design changes to the detector as well, especially when it comes to the forward region. The details of the endcap geometry and its interplay with the barrel region have not been be the focus of this work and will be optimized in the future. The placement of the transition region will depend heavily on the character of the BIB, the energy of the collisions, and the physics processes of interest.

The overall layout of the entire silicon tracker can also be reoptimized. We aim to explore the use of double layers in the inner and outer tracker designs paired with a redesign of the overall geometry, potentially using machine learning to optimize the many parameters of the tracker layout. Double layers have been studied in the past in the context of a muon collider experiment, but we aim to study their utility in the outer layers of the tracking system. In the tracker endcaps, we will explore the use of tilted geometries to reduce the average angle of incidence, making better use of the high spatial resolution of the modules and reducing the average cluster size.

The muon system currently largely operates as a tagger, bypassing the need for an additional magnet to form a spectrometer. Given that this tracker-based design provides a binary tagger, building muon tagging abilities into the design of the calorimeter may completely remove the need for a dedicated muon detection system. We aim to explore the use of HCAL technologies that use micropattern gaseous detectors [48] with single-particle tracking abilities to simultaneously act as an HCAL and a muon tagger. Such a technology could be used in tandem with the iron-scintillator design presented here for a hybrid HCAL system.

A dedicated feasibility study is required for the solenoid. In these studies, we have assumed a 5T magnet with an inner radius of 150 cm simulated as a region of high-density materials, aluminum and steel. The feasibility of such a magnet needs to be evaluated, particularly given the sensitivity of the calorimetry to the amount of material in the magnet. A more realistic model of such a large high-field magnet should incorporate radiation tolerance requirements, and the structural and material design must be able to handle the large mechanical stresses from the field.

Future work includes a deeper analysis of detector backgrounds. While the central background dictating the design of the detector is from the decay of beam muons, additional sources of background particles and hits exist. At a collision energy of 10 TeV, processes

involving radiated photons from the beam particles become sizeable, particularly in the in-coherent production of electrons. Muonic Bhabha scattering will also lead to soft particle production in the detector. Since such particles can emerge from the interaction region, they can evade the background reduction that comes from tracking, particle flow, or angular projectivity requirements.

A goal of such an experiment is to be able to run in a triggerless manner. The feasibility of this goal heavily depends on the machine parameters, the level of background, and the ability to read out the detector at the full collision rate. Preliminary studies suggest that triggerless readout may be possible with this concept, but more mature data throughput studies would be required to demonstrate this feasibility. One potential area of concern is the vertex layers of the silicon tracker, which would see the highest occupancy rates overall and require the most bandwidth for readout.

The algorithms used in the results presented here have been coarsely optimized for rea-sonable performance. The performance is expected to greatly benefit from additional al-gorithmic optimizations for many of the physics objects discussed here. Improved photon reconstruction in the presence of BIB is crucial for many of the of the physics goals at such a machine, and reconstructed photons that arise purely from BIB contributions are not yet studied here. Since the high-dimensional shower shape in the ECAL is the only handle for photons, photon reconstruction is an ideal case for machine learning discriminators given the large effect of BIB on the ECAL. The optimization of the tracking algorithm may need to be reevaluated given the additional detector backgrounds discussed above.

We also leave the study of higher level physics objects for future work. Flavor tagging of jets will serve as an important tool, particularly for the program of studying the Higgs boson and new physics that couples to heavy flavor. Flavor tagging of jets requires a careful interplay of tracker and calorimeter measurements and will be better understood as the more fundamental reconstruction algorithms improve in sophistication. The same is true for the identification of hadronically decaying τ leptons.

The particle flow algorithm provided by the Pandora package is not well optimized for this unique muon collider environment, and achieving a useful particle flow algorithm will require significant high-level reconstruction studies once basic objects are very well understood.

In addition to these lower-level improvements, studies of the overall physics performance are necessary, especially in the presence of a sophisticated suite of backgrounds. Studies of

the multi-object mass resolutions, missing energy measurement performance, and primary and secondary vertex reconstruction are crucial to ensuring robust physics performance from the experiment. Dedicated studies of full signal processes in the presence of realistic backgrounds are required to characterize the reach for standard model measurements and in searches for physics beyond the standard model.

VII. CONCLUSIONS

The MAIA detector concept shows considerable promise in advancing our capability to conduct precision and discovery physics at a 10 TeV muon collider. Here, track, photon, and neutron measurements showcase the excellent reconstruction capability of the tracker, ECAL, and HCAL: under realistic BIB conditions, we observe minimal degradation in performance for energetic particles in the central region of the detector. Track reconstruction efficiencies with BIB exceed 95% in the barrel, and track p_{T} and impact parameter resolutions approach 0.1% and 3 μm, respectively. For photons with E > 100 GeV in the presence of BIB, reconstruction efficiencies surpass 95% throughout the central barrel and endcap, with energy resolutions approaching 0.5%. Energetic neutral hadrons (E > 300 GeV) in the barrel feature reconstruction efficiencies greater than 95% and energy resolutions better than 10%. A critical driver of this performance is several ps-scale timing resolutions and high-granularity calorimetry.

This work establishes a baseline detector concept for physics studies at a 10 TeV muon collider and proposes several directions for future work. Priorities include re-optimizing the tracker layout, especially in the endcap and forward regions, investigating advanced calorimetry technologies, and determining whether a dedicated muon system is essential for muon reconstruction. Additionally, developing and testing reconstruction algorithms for other physics objects, including electrons, taus, heavy flavor jets, and missing transverse momentum, along with adapting these algorithms as the detector layout evolves, is vital. We intend to continue to explore many of these avenues in future work.

Acknowledgments

---

[1] SLAC-SP-017 Collaboration, "Discovery of a Narrow Resonance in e^+e^- Annihilation", *Phys. Rev. Lett.* **33** (1974) 1406–1408, doi:10.1103/PhysRevLett.33.1406.

[2] E598 Collaboration, "Experimental Observation of a Heavy Particle J", *Phys. Rev. Lett.* **33** (1974) 1404–1406, doi:10.1103/PhysRevLett.33.1404.

[3] ATLAS Collaboration, "Observation of a new particle in the search for the Standard Model Higgs boson with the ATLAS detector at the LHC", *Phys. Lett. B* **716** (2012), no. 1, 1 – 29, doi:https://doi.org/10.1016/j.physletb.2012.08.020.

[4] CMS Collaboration, "Observation of a New Boson at a Mass of 125 GeV with the CMS Experiment at the LHC", *Phys. Lett. B* **716** (2012) 30–61, doi:10.1016/j.physletb.2012.08.021, `arXiv:1207.7235`.

[5] T. Roser et al., "On the feasibility of future colliders: report of the Snowmass'21 Implementation Task Force", *Journal of Instrumentation* **18** (May, 2023) P05018, doi:10.1088/1748-0221/18/05/p05018.

[6] C. Aimè et al., "Muon Collider Physics Summary", 2022. `https://arxiv.org/abs/2203.07256`.

[7] C. Accettura et al., "Towards a Muon Collider", 2023. `https://arxiv.org/abs/2303.08533`.

[8] J. P. Delahaye et al., "Muon Colliders", 2019. `https://arxiv.org/abs/1901.06150`.

[9] K. Long et al., "Muon colliders to expand frontiers of particle physics", *Nature Phys.* **17** (2021), no. 3, 289–292, doi:10.1038/s41567-020-01130-x, `arXiv:2007.15684`.

[10] J.-P. Delahaye et al., "A Staged Muon Accelerator Facility For Neutrino and Collider Physics", 2015. `https://arxiv.org/abs/1502.01647`.

[11] D. Lucchesi et al., "Detector Performances Studies at Muon Collider", *PoS* **EPS-HEP2019** (2020) 118, doi:10.22323/1.364.0118.

[12] C. M. Ankenbrandt et al., "Status of muon collider research and development and future plans", *Phys. Rev. ST Accel. Beams* **2** (1999) 081001, doi:10.1103/PhysRevSTAB.2.081001, `arXiv:physics/9901022`.

[13] M. Boscolo, J.-P. Delahaye, and M. Palmer, "The future prospects of muon colliders and neutrino factories", *Rev. Accel. Sci. Tech.* **10** (2019), no. 01, 189–214, doi:10.1142/9789811209604_0010, `arXiv:1808.01858`.

[14] D. Neuffer et al., "Muon Sources for Particle Physics - Accomplishments of MAP", in *Proc. of International Particle Accelerator Conference (IPAC'17), Copenhagen, Denmark, 14-19 May, 2017*, number 8 in International Particle Accelerator Conference, pp. 1766–1769. JACoW, Geneva, Switzerland, May, 2017. https://doi.org/10.18429/JACoW-IPAC2017-TUPIK038. doi:https://doi.org/10.18429/JACoW-IPAC2017-TUPIK038.

[15] N. Bartosik et al., "Full Detector Simulation with Unprecedented Background Occupancy at a Muon Collider", *Comput. Softw. Big Sci.* **5** (2021), no. 1, 21,

doi:10.1007/s41781-021-00067-x.

[16] C. Accettura et al., "Towards a muon collider", *Eur. Phys. J. C* **83** (2023), no. 9, 864, doi:10.1140/epjc/s10052-023-11889-x, `arXiv:2303.08533`. [Erratum: Eur.Phys.J.C 84, 36 (2024)].

[17] P. Fernandez Declara et al., "The Key4hep turnkey software stack for future colliders", *PoS* **EPS-HEP2021** (2022) 844, doi:10.22323/1.398.0844.

[18] Key4hep Collaboration, A. Sailer et al., "The Key4hep software stack: Beyond Future Higgs factories", in *21th International Workshop on Advanced Computing and Analysis Techniques in Physics Research: AI meets Reality.* 12, 2023. `arXiv:2312.08151`.

[19] M. Frank, F. Gaede, C. Grefe, and P. Mato, "DD4hep: A Detector Description Toolkit for High Energy Physics Experiments", *J. Phys. Conf. Ser.* **513** (Oct, 2013) 022010, doi:10.1088/1742-6596/513/2/022010.

[20] S. Agostinelli et al., "GEANT4 - A Simulation Toolkit", *Nucl. Inst. & Meth.* **A506** (2003) 250–303, doi:10.1016/S0168-9002(03)01368-8.

[21] M. Petric et al., "Detector Simulations with DD4hep", *J. Phys. Conf. Ser.* **898** (2016), no. 4, 042015, doi:10.1088/1742-6596/898/4/042015.

[22] F. Gaede, T. Behnke, N. Graf, and T. Johnson, "LCIO: A Persistency framework for linear collider simulation studies", *eConf* **C0303241** (2003) TUKT001, doi:10.48550/arXiv.physics/0306114, `arXiv:physics/0306114`.

[23] F. Gaede et al., "EDM4hep and podio - The event data model of the Key4hep project and its implementation", *EPJ Web Conf.* **251** (2021) 03026, doi:10.1051/epjconf/202125103026.

[24] "ILC Soft". `https://github.com/iLCSoft`.

[25] F. Gaede, "Marlin and LCCD: Software tools for the ILC", *Nucl. Inst. & Meth.* **A559** (2006) 177–180, doi:10.1016/j.nima.2005.11.138.

[26] R. Fruhwirth, "Application of Kalman filtering to track and vertex fitting", *Nucl. Instrum. Meth. A* **262** (1987) 444–450, doi:10.1016/0168-9002(87)90887-4.

[27] P. Billoir, "Track Fitting With Multiple Scattering: A New Method", *Nucl. Instrum. Meth. A* **225** (1984) 352–366, doi:10.1016/0167-5087(84)90274-6.

[28] P. Billoir and S. Qian, "Further test for the simultaneous pattern recognition and track fitting by the Kalman filtering method", *Nucl. Instrum. Meth. A* **295** (1990) 492–500, doi:10.1016/0168-9002(90)90731-K.

[29] X. Ai et al., "A Common Tracking Software Project", *Comput. Softw. Big Sci.* **6** (2022), no. 1, 8, doi:10.1007/s41781-021-00078-8, `arXiv:2106.13593`.

[30] G. Battistoni et al., "Overview of the FLUKA code", *Annals of Nuclear Energy* **82** (2015) 10–18, doi:https://doi.org/10.1016/j.anucene.2014.11.007. Joint International Conference on Supercomputing in Nuclear Applications and Monte Carlo 2013, SNA + MC 2013. Pluri- and Trans-disciplinarity, Towards New Modeling and Numerical Simulation Paradigms.

[31] C. Ahdida et al., "New Capabilities of the FLUKA Multi-Purpose Code", *Frontiers in Physics* **9** (2022) doi:10.3389/fphy.2021.788253.

[32] D. Calzolari, "Status of the background and forward muon studies for the 10 TeV collider", 2023. `https://indico.cern.ch/event/1250075/contributions/5342843/`.

[33] I. F. Ginzburg, "The e^+e^- pair production at $\mu^+\mu^-$ collider", 1996.

[34] D. Schulte, "Beam-Beam Simulations with GUINEA-PIG", 1998. `https://cds.cern.ch/record/382453`.

[35] K. Skoufaris, C. Carli, and D. Schulte, "10 TeV Center of Mass Energy Muon Collider", in *Proc. IPAC'22*, number 13 in International Particle Accelerator Conference, pp. 515–518. JACoW Publishing, Geneva, Switzerland, 7, 2022. doi:10.18429/JACoW-IPAC2022-MOPOTK031.

[36] N. V. Mokhov et al., "Muon Collider interaction region and machine-detector interface design", 2012.

[37] C. Curatolo et al., "Monte Carlo Driven MDI Optimization at a Muon Collider", in *Proc. IPAC'21*, pp. 3769–3772. JACoW Publishing, Geneva, Switzerland, 2021. doi:10.18429/JACoW-IPAC2021-THPAB011.

[38] D. Calzolari and K. Skoufaris, "SISSA: Machine-detector interface studies for a multi-TeV muon collider", *PoS* (2022) 063.

[39] D. Calzolari et al., "JACOW: Lattice and detector studies for the MDI of a 10 TeV muon collider", *JACoW IPAC* **2023** (2023) MOPA090.

[40] ATLAS Collaboration, "A High-Granularity Timing Detector for the ATLAS Phase-II Upgrade: Technical Design Report",.

[41] CMS Collaboration, "A MIP Timing Detector for the CMS Phase-2 Upgrade",.

[42] Muon Collider Collaboration, "Promising Technologies and R&D Directions for the Future Muon Collider Detectors", `arXiv:2203.07224`.

[43] A. Robson et al., "The Compact Linear e^+e^- Collider (CLIC): Accelerator and Detector", 2018. https://arxiv.org/abs/1812.07987.

[44] CMS Collaboration, "The Phase-2 Upgrade of the CMS Endcap Calorimeter", technical report, CERN, Geneva, 2017. doi:10.17181/CERN.IV8M.1JY2.

[45] ATLAS Collaboration, "ATLAS tile calorimeter: Technical design report", technical report, CERN, 12, 1996.

[46] J. S. Marshall and M. A. Thomson, "The Pandora Software Development Kit for Particle Flow Calorimetry", *Journal of Physics: Conference Series* **396** (dec, 2012) 022034, doi:10.1088/1742-6596/396/2/022034.

[47] M. Paganini, L. de Oliveira, and B. Nachman, "CaloGAN : Simulating 3D high energy particle showers in multilayer electromagnetic calorimeters with generative adversarial networks", *Phys. Rev. D* **97** (2018), no. 1, 014021, doi:10.1103/PhysRevD.97.014021, arXiv:1712.10321.

[48] A. Pellecchia et al., "Design and optimization of a hadronic calorimeter based on micropattern gaseous detectors for a future experiment at the Muon Collider", *Nucl. Instrum. Meth. A* **1068** (2024) 169793, doi:10.1016/j.nima.2024.169793, arXiv:2407.10261.

[49] R. Pordes et al., "The open science grid", in *J. Phys. Conf. Ser.*, volume 78 of *78*, p. 012057. 2007. doi:10.1088/1742-6596/78/1/012057.

[50] I. Sfiligoi et al., "The pilot way to grid resources using glideinWMS", in *2009 WRI World Congress on Computer Science and Information Engineering*, volume 2 of *2*, pp. 428–432. 2009. doi:10.1109/CSIE.2009.950.

[51] OSG, "OSPool", 2006. doi:10.21231/906P-4D78, https://osg-htc.org/services/open_science_pool.html.

[52] OSG, "Open Science Data Federation", 2015. doi:10.21231/0KVZ-VE57, https://osdf.osg-htc.org/.